Strong Quantum Confinement and Fast Photoemission Activation in $CH_3NH_3PbI_3$ Perovskite Nanocrystals Grown within Periodically Mesostructured Films

*Miguel Anaya, Andrea Rubino, Teresa Cristina Rojas, Juan Francisco Galisteo-López, Mauricio Ernesto Calvo, and Hernán Míguez**

In this Communication, a synthetic route is demonstrated to obtain stabilized $MAPbI_3$ nanocrystals embedded in thin metal oxide films that display well-defined and adjustable quantum confinement effects over a wide range of 0.34 eV. Mesostructured TiO_2 and SiO_2 films displaying an ordered 3D pore network are prepared by evaporation-induced self-assembly of a series of organic supramolecular templates in the presence of metal oxide precursors. The pores in the inorganic films obtained after thermal annealing are then used as nanoreactors to synthesize $MAPbI_3$ crystallites with narrow size distribution and average radius comprised between 1 and 4 nm, depending on the template of choice. Both the static and dynamic photoemission properties of the ensemble display features distinctive of the regime of strong quantum confinement. Photoemission maps demonstrate that the spectral and intensity properties of the luminescence extracted from the perovskite quantum dot loaded films are homogeneous over squared centimeters areas. At variance with their bulk counterparts, constant emission intensity is reached in time scales at least four orders of magnitude shorter.

One of the most versatile strategies to tune the optical properties of a semiconductor consists in reducing its size until it becomes of the order of the exciton Bohr radius and quantum confinement effects arise.[1] Different methods have been developed to try to controllably diminish the size of methyl ammonium lead halide ($MAPbX_3$, X = Cl, Pb, I) crystals,[2–7] motivated by the interest these perovskites generate in the field of optoelectronics.[8–12] Efforts in obtaining dispersions of hybrid organic–inorganic perovskite nanocrystals for optoelectronic applications have mainly focused on $MAPbBr_3$ and $MAPbBr_xI_{3-x}$, as this allows achieving visible emission bands. $MAPbI_3$, on the other hand, is an efficient near infrared emitter and presents a lower lasing threshold than $MAPbBr_3$.[13] Evidence of precise control of the optical properties of $MAPbI_3$ over a wide spectral range has been reported from colloidal suspensions attained using a two-step process involving the synthesis of PbI_2 nanocrystals and their subsequent reaction with $CH_3NH_3I_3$ to produce the corresponding organic–inorganic lead halide quantum dots.[4] More recently, powders of porous silica exhibiting a 2D hexagonal mesopore structure have been used as templates to synthesize $MAPbI_3$ nanocrystals.[14,15] This approach proved to be suitable to attain bright and stable emission whose spectrum could be controlled by the average pore size of the matrix. However, most applications foreseen for hybrid perovskites require the use of thin films of high optical quality, as well as versatility regarding the composition of the scaffold employed. In order to achieve this goal, mesostructures with geometries other than the hexagonal one previously employed to host perovskite nanocrystals must be used, since the characteristic tubular channels tend to lie parallel to the substrate when the porous material is shaped as a film, becoming inaccessible from the top surface. This prevents their infiltration with perovskite precursors. Very recently, $MAPbI_2X$ (X = Cl, Br, I) compounds have been synthesized inside metal organic framework films,[16] but no control over the size and optical properties of $MAPbI_3$ was demonstrated.

In this Communication, we demonstrate a synthetic route to obtain stabilized $MAPbI_3$ nanocrystals embedded in thin metal oxide films that display well-defined and adjustable quantum confinement effects over a wide range of 0.34 eV. Mesostructured TiO_2 and SiO_2 films displaying an ordered 3D pore network are prepared by evaporation induced self-assembly of a series of organic supramolecular templates in the presence of metal oxide precursors. The pores in the inorganic films obtained after thermal annealing are then used as nanoreactors to synthesize $MAPbI_3$ crystallites with narrow size distribution and average radius comprised between 1 and 4 nm, depending on the template of choice. Both the static and dynamic photoemission properties of the ensemble display features distinctive of the regime of strong quantum confinement. Photoemission maps demonstrate that the spectral and intensity properties of the luminescence extracted from the perovskite quantum dot loaded films are homogeneous over squared centimeters areas. In addition, the photoemission stationary state is reached 10^4 times faster than in a $MAPbI_3$ solid film.

M. Anaya, A. Rubino, Dr. T. C. Rojas,
Dr. J. F. Galisteo-López, Dr. M. E. Calvo, Prof. H. Míguez
Institute of Materials Science of Seville
Spanish National Research Council-University of Seville
Calle Américo Vespucio 49, 41092 Seville, Spain
E-mail: h.miguez@csic.es

DOI: 10.1002/adom.201601087

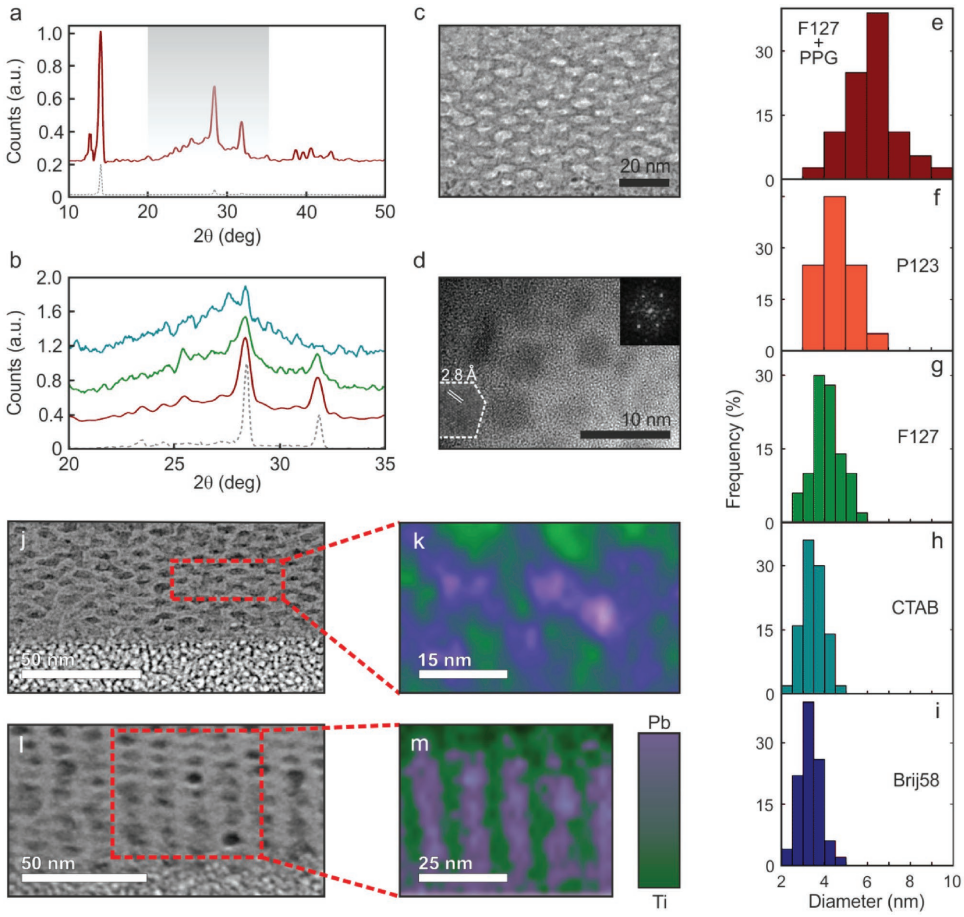

Figure 1. a) XRD pattern of $CH_3NH_3PbI_3$ grown within an F127 + PPG-templated TiO_2 mesostructured scaffold. b) XRD patterns detail of the peak broadening corresponding to {220} reflections of $CH_3NH_3PbI_3$ crystals grown in a flat substrate, and within F127 + PPG- (red), F127- (green), and CTAB- (blue–green) templated TiO_2 mesostructured scaffolds. Gray dashed curves indicate the reference pattern of tetragonal phase bulk $CH_3NH_3PbI_3$ perovskite. c) High-magnification transmission electron microscopy image of a cross section of an F127 + PPG-templated TiO_2 mesostructured scaffold. d) High-resolution transmission electron microscopy image showing the crystalline planes of different $CH_3NH_3PbI_3$ nanocrystals. Inset displays the digital diffraction pattern of the highlighted particle. Size distribution histograms of $CH_3NH_3PbI_3$ nanocrystals grown within different porous TiO_2 scaffolds in which the voids are ordered by using e) F127 + PPG, f) P123, g) F127, h) CTAB, and i) Brij58 as organic template agent. HAADF-STEM image of a j) hexagonal-, and l) cubic-like pore distribution which can be assigned to different cross section planes of an F127-templated mesostructured scaffold infiltrated by $CH_3NH_3PbI_3$. XEDS chemical maps of Ti and Pb obtained from the marked regions, for both k) hexagonal- and m) cubic-like ordered pore planes infiltrated by $CH_3NH_3PbI_3$.

In order to create a stable solid dispersion of $MAPbI_3$ quantum dots, we follow a standard one-step procedure that starts by dissolving precursors in *N*,*N*-dimethylformamide.[5] The solution is then spin coated onto periodically mesostructured metal oxide, namely, TiO_2 or SiO_2, films of controlled thickness and open porosity, which have been previously deposited on flat glass substrates by a combination of supramolecular templating and dip-coating.[17] Precursor concentration is a critical parameter in order to ensure that the perovskite is grown exclusively within the film pores and to prevent the formation of a bulk perovskite capping layer (Figure S1, Supporting Information). Filling of the void network and subsequent thermal annealing give rise to the formation of $MAPbI_3$ crystallites, as revealed by X-ray diffraction (XRD) and high-resolution transmission electron microscopy (HRTEM) images taken from the cross sections of thin lamellae prepared by focused ion beam. Analysis of the X-ray diffractograms, like the one displayed in **Figure 1**a, demonstrates that the stable phase of the crystallites within the cages is tetragonal, which implies that the final structure achieved is the same one observed in bulk $MAPbI_3$ films. As the pore size decreases, the characteristic diffraction peak intensities lower and widen, as shown in Figure 1b. By using Scherrer formula, it is only possible to roughly guess that perovskite crystal size varies, among the different films prepared, in the range of a few nanometers, as the low intensity of the diffraction maxima prevents a finer estimation. On the other hand, arrays of crystallites of similar size and shape, synthesized within porous TiO_2 matrices like that shown in Figure 1c, can be readily identified on HRTEM images, as illustrated in Figure 1d. Interplanar distances corresponding to the tetragonal structure of $MAPbI_3$ are recognized, as shown in the inset of this figure. The nanocrystal size distributions, extracted from the analysis of the HRTEM images, corresponding to each one of the $MAPbI_3$ filled mesostructured films are presented

in Figure 1e–i. The estimated crystallite average size correlates with the average pore size expected in each film, which is determined to a good extent by the organic supramolecular template employed. Hence, crystals of radii $R = 3.10 \pm 0.08$ nm, $R = 2.26 \pm 0.03$ nm, $R = 2.03 \pm 0.07$ nm, $R = 1.70 \pm 0.05$ nm, and $R = 1.64 \pm 0.02$ nm are observed inside the void lattice of films made using, respectively, a mixture of F127 and PPG, P123, F127, cethyltrimethylammonium bromide (CTAB), and Brij58 as surfactants (full details on composition are provided in the Experimental Section). Elemental analysis performed by means of energy-dispersive X-ray spectroscopy (EDX) was used to study the spatial distribution of Pb and Ti inside the mesostructured film. Those elemental maps and the corresponding high angle annular dark field scanning TEM (HAADF-STEM) images are displayed in Figure 1j–m. In this specific case, they were attained from two different inner surfaces of the ordered pore lattice filled with $MAPbI_3$ crystallites. Interestingly, these observations ratify that the $MAPbI_3$ crystallites array inherits the order of the pore network in which it is formed, although this has no apparent effect on the optical response of the ensemble. These results confirm that the periodically ordered films can be efficiently infiltrated by means of successive impregnation with the $MAPbI_3$ precursors.

The most direct consequence of the confinement of a semiconductor is the quantization of its energy levels and the enlargement of its electronic band gap, which reveals itself in the spectral blueshift of both its optical absorption edge and the corresponding luminescence peak. Hence the optical properties of the crystallite networks built in periodically mesostructured scaffolds were investigated by analyzing their photoluminescence (PL) and photoexcitation (PE) spectra. Results are shown in **Figure 2**a. A single peak at a wavelength of $\lambda_0 = 775$ nm ($E_g = 1.60$ eV) was detected in the PL spectrum of the scaffold-free $MAPbI_3$ film used for comparison, which corresponds to the photoemission peak already reported for the bulk $MAPbI_3$ perovskite.[5] Crystallites synthesized within periodically porous films displayed PL peaks at $\lambda_0 = 692$ nm ($E_0 = 1.79$ eV), $\lambda_0 = 686$ nm ($E_0 = 1.81$ eV), $\lambda_0 = 677$ nm ($E_0 = 1.83$ eV), $\lambda_0 = 660$ nm ($E_0 = 1.88$ eV), and $\lambda_0 = 638$ nm ($E_0 = 1.94$ eV), where the surfactant employed to achieve each one of the mesostructures is indicated. This implies a maximum blueshift of $\Delta\lambda_0 = 137$ nm ($\Delta E_0 = 0.34$ eV), one of the largest so far reported for $MAPbI_3$ crystallites. Simultaneously, a consistently similar shift is observed at the edge of the photoexcitation spectra.

The spectral displacement observed in both photoemission and photoexcitation spectra increases as the average crystallite size present in the film decreases, as expected for a semiconductor in which quantum confinement of electron–hole pairs takes place. In fact, the comparison between the crystal radii measured by HRTEM and the reported estimated values of Bohr radius ($R_B \approx 3$ nm),[18–22] which yields $\frac{R}{R_B} < 2$ in all cases, as well as the magnitude of the bandgap shift observed for $MAPbI_3$ nanocrystals ($\Delta E_0 = 0.34$ eV), indicate that our observations may be well explained assuming a strong confinement regime, after the classification established by Kayanuma.[23] Within this regime, both electron and hole are expected to be found mainly occupying their respective lowest energy

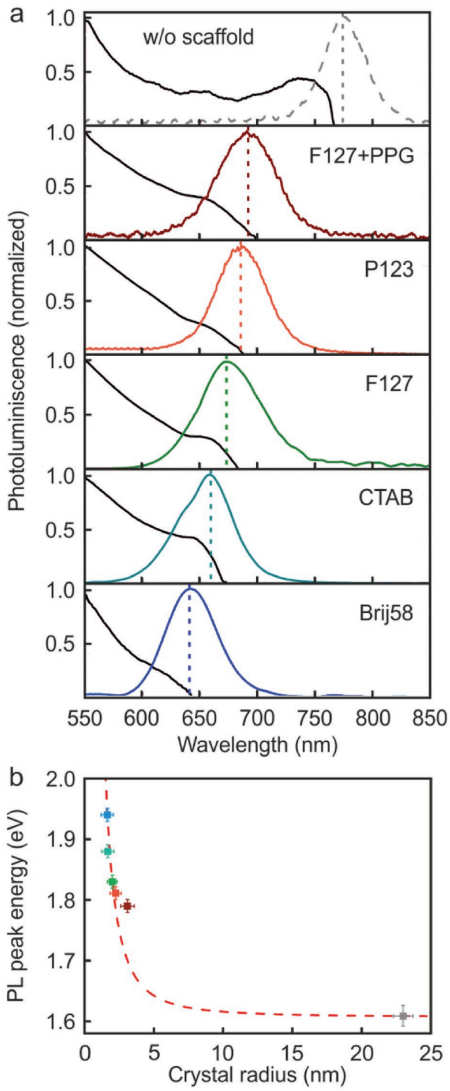

Figure 2. a) Normalized PL and PE (colored and black lines, respectively) spectra from $CH_3NH_3PbI_3$ nanocrystals grown in a low-fluorescence glass without scaffold (gray), and with supramolecularly templated TiO_2 scaffolds F127 + PPG (dark red), P123 (orange), F127 (green), CTAB (blue–green), and Brij58 (blue). Colorful dashed lines are displayed as a guide to the eye to locate the wavelengths at which PL peaks in each case. b) Spectral position of the PL peak maxima with respect to the crystal radius of the $CH_3NH_3PbI_3$ nanocrystals grown within the different TiO_2 scaffolds (color code is preserved from (a)). The best fit to Brus equation is also plotted as a red dashed line.

eigenstates and with little spatial correlation between them. In order to provide a deeper insight on the nature of the effects observed, we analyzed the dependence between the size of the crystals and their photoluminescence properties. In Figure 2b we plot the energy (eV) at which PL maxima are detected versus the crystal size as estimated from the HRTEM analysis. Superimposed, we draw the curve (dashed line) corresponding to the best fit of our data to the equation

$$E_0 \approx E_g + \frac{h^2}{8\mu R^2} - \frac{1.786e^2}{4\pi\varepsilon_0\varepsilon_r R} \quad (1)$$

usually known as Brus formula,[24] which assumes a hydrogen-like model to describe the interaction between electron–hole pairs strongly confined in spherical semiconductor nanocrystals.[23,25] In this expression, E_0 is the energy of the lowest excited state of the exciton inside the nanocrystal, E_g is the energy bandgap of bulk $MAPbI_3$ (in our case 1.60 eV), h is Planck's constant, μ is the exciton reduced mass, R is the radius of the nanoparticle, e is the electron charge, and ε_0 and ε_r are the dielectric constants of vacuum and $MAPbI_3$, respectively. The second term on the right-hand side of the equation has a kinetic origin and corresponds to the first energy level of a quasiparticle of reduced mass μ confined in a spherical well of radius R limited by a wall of infinite potential. The third term on that same side of the equation is known as the Coulomb energy term, as it arises from considering the electrostatic interaction between the electron and the hole confined in the nanocrystal. Its contribution, although less significant than that of the kinetic term due to both the high screening of the interaction in high dielectric constant semiconductors like $MAPbI_3$ and the fact that it scales like R^{-1} instead of R^{-2}, cannot be neglected. From the fitting of our experimental data, we can estimate an exciton reduced mass of $\mu = 0.27 \pm 0.01$ m_0, with m_0 being the electron rest mass, and a dielectric constant of $\varepsilon_r = 18.0 \pm 0.5$. From them, we can make use of the following relations between the exciton binding energy, E_B, and Bohr radius, R_B

$$E_B = \frac{\mu}{m_0}\cdot\frac{1}{\varepsilon_r^2}\cdot\frac{m_0 e^4}{2(4\pi\varepsilon_o\hbar)^2} = \frac{\mu}{m_0}\cdot\frac{1}{\varepsilon_r^2}\cdot E_{B_{hydrogen}} = \frac{\mu}{m_0}\cdot\frac{1}{\varepsilon_r^2}\cdot 13.6 \quad (2)$$

$$R_B = \frac{m_0}{\mu}\cdot\varepsilon_r\cdot R_{B_{hydrogen}} = \frac{m_0}{\mu}\cdot\varepsilon_r\cdot 0.053 \quad (3)$$

to obtain $E_B = 11.3 \pm 1.0$ meV and $R_B = 3.53 \pm 0.23$ nm for $MAPbI_3$. This set of values for μ, ε_r, E_B, and R_B are in fair agreement with previously reported ones based on theoretical estimations that have been demonstrated to reproduce well the behavior of bulk $MAPbI_3$ at room temperature.[19,22,26–28] This agreement supports the validity of the use of Brus approximation to describe the observed trends, although it should be taken into account that, in this expression, the effective mass is considered to be independent of the crystal size, an approximation that might not necessarily hold for extremely small crystallites.

From the point of view of the material performance, the nanocrystal loaded films present an emission detectable with the naked eye in spite of being only 200 nm thick, as it can be seen in the picture displayed in **Figure 3**a. This photograph was taken under monochromatic light excitation of $\lambda = 312$ nm from a porous TiO_2 film in which 2.26 nm size $MAPbI_3$ nanocrystals were synthesized. Bright edges result from the guiding of the emitted light by the glass substrate. Tracking the time evolution of the PL peak from the nanostructured film we observe that 10 ms (limited by the time resolution of our set-up) after the excitation of the film it reaches a stable emission (Figure 3b). This is in contrast with the slow photoactivation of the PL

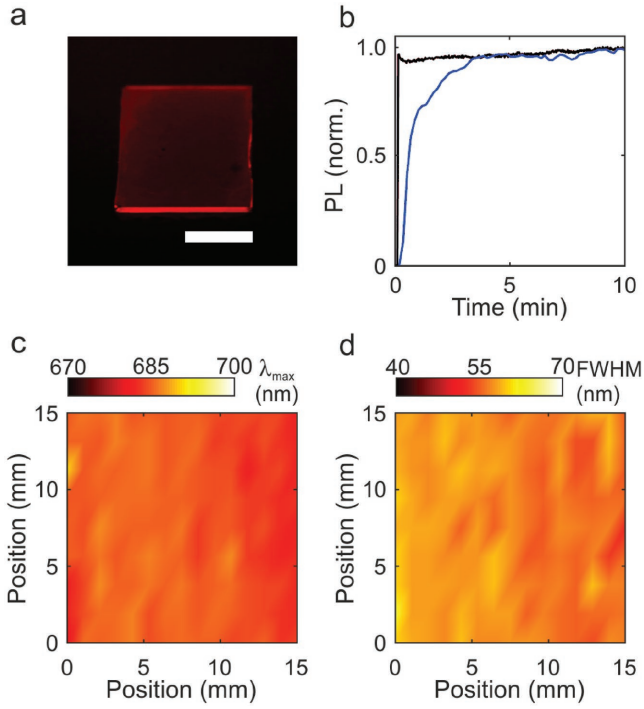

Figure 3. a) Digital camera picture of a periodically ordered porous film (P123) containing $MAPbI_3$ nanocrystals taken under illumination with UV light of $\lambda = 312$ nm. Scale bar is 1 cm. b) Photoluminescence maximum of confined $MAPbI_3$ nanocrystals ($\lambda_{max} = 684$ nm, black curve) and a bulk $MAPbI_3$ film ($\lambda_{max} = 775$ nm, blue curve) as a function of time under excitation with monochromatic light of $\lambda = 532$ nm. Maps of the c) photoluminescence maximum and d) FWHM over the 2.25 cm^2 surface of a porous film containing $MAPbI_3$.

presented by a bulk film of similar thickness (i.e., 200 nm). Such slow dynamics of the PL of bulk $MAPbI_3$ has been previously observed in the past,[29,30] and has been proposed to originate at trap-filling caused by the photoinduced migration of ions within the perovskite lattice under illumination.[31] Within this picture it is reasonable to assume that the time needed for ions to traverse the size of the nanocrystal should be orders of magnitude smaller than that for the bulk case. This observation suggests that, under similar excitation conditions, the PL of nanocrystals enters the so-called bimolecular regime, in which carrier decay rate is dominated by radiative recombination,[32] much faster than that of bulk crystals, which remains for longer in the monomolecular regime, in which nonradiative trap filling prevails. Furthermore, the confined perovskite nanocrystals are as stable as the bulk perovskite films. Indeed, they conserve their emission properties over weeks although they are conserved under dark ambient conditions. In order to evaluate the homogeneity of the emission, the PL spectrum was measured from 250 μm^2 regions, mapping the whole film surface (2.25 cm^2). The maps obtained reveal the high regularity of the nanocrystal size distribution and density over the entire film, as it can be seen in Figure 3c,d. Luminescence peak maximum (λ_{max}) and full width at half maximum (FWHM) remains practically constant within very narrow margins, $\lambda_{max} = 684 \pm 2$ nm (i.e., 1.81 eV, standard deviation 0.3%) and FWHM = 57 ± 2 nm (i.e., 0.15 eV, standard deviation 3.5%).

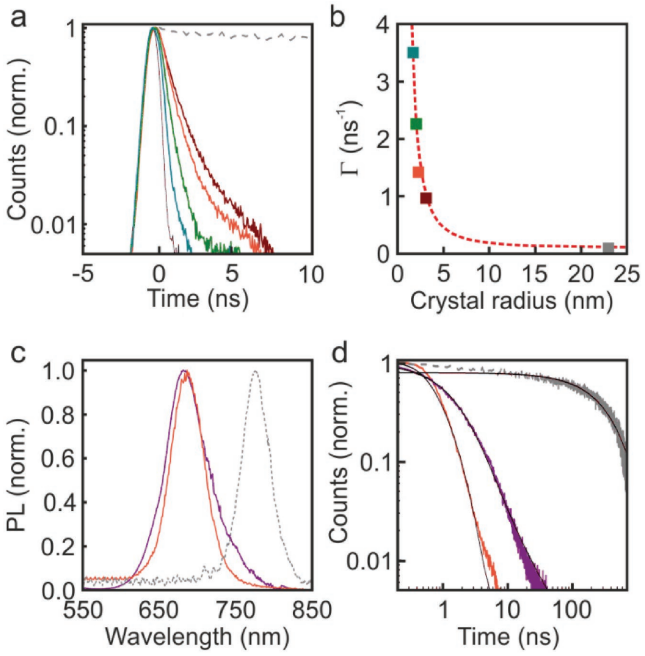

Figure 4. a) Normalized PL decay curves for the $CH_3NH_3PbI_3$ formed within supramolecularly templated mesoporous TiO_2 scaffolds by using CTAB (blue–green), F127 (green), P123 (orange), and F127 + PPG (dark red) as organic template. Gray dashed line belongs to a reference flat perovskite film. Black solid line indicates the instrument response function (IRF) produced by the excitation pulse. b) PL decay rate versus the frequency at which the PL is maxima for the $CH_3NH_3PbI_3$ infiltrated in the different scaffolds (color code is preserved from (a)). The red dashed line is the best fitting curve following an inversely quadratic dependence with crystal radius. c) Normalized PL spectra from $CH_3NH_3PbI_3$ nanocrystals of similar size grown using supramolecularly templated TiO_2 (orange) and SiO_2 (purple) porous films as scaffolds. Gray dashed line corresponds to the photoemission spectrum of a flat perovskite film. d) Corresponding normalized decay curves for the $CH_3NH_3PbI_3$ formed within both type of scaffolds (color code is preserved from (c)).

Electron–hole pairs confined in nanosized semiconductors are also expected to experience significant modifications in their decay dynamics.[33] We have performed time resolved PL measurements for the series of $MAPbI_3$ crystallites prepared, as well as for a bulk perovskite film, for the sake of comparison. A 532 nm excitation wavelength was employed in all cases, and the time evolution of the emitted intensity was monitored by means of time correlated single photon counting within a 5 nm wide spectral window centered at the respective emission maximum. Results shown in **Figure 4**a are representative of each type of sample, since very similar curves were systematically obtained from different regions of the same film. It can be readily seen that the average excited state lifetime τ_{av} decreases, hence decay rate Γ accelerates, as the crystal size is reduced. Data analysis of each curve revealed that the PL decays are best fitted to a normal distribution of lifetimes (see Figure S2, Supporting Information). A comparative analysis of the widths of the lifetime distributions and those of the $MAPbI_3$ quantum dot size distributions, obtained from Figure 1e–i, shows the absence of correlation between them. This implies that the lifetime distribution cannot be exclusively the result of the dispersion observed in quantum dot size, but also of the effect of other nonradiative processes. Measurements of the quantum yield (QY) return values of QY ≈ 1%, very similar to those previously reported for other confined $MAPbI_3$ nanocrystals.[14,15] Since $QY = \frac{\Gamma_R}{\Gamma} = \frac{\Gamma_R}{\Gamma_{NR}+\Gamma_R}$, where Γ_{NR} and Γ_R are the nonradiative and radiative decay rates respectively, our QY measurements show that nonradiative processes are dominant over radiative ones, i.e., $\Gamma_{NR} >> \Gamma_R$. Simultaneously, an analysis of the dependence of the mean decay rate estimated from the PL decay curves with the average nanocrystal radius reveals that $\Gamma \sim R^{-2}$. Hence, in our case, Γ_{NR} is inversely proportional to the area of the nanocrystal surface. This could be due to the fact that the smaller the crystal, the larger the surface lattice distortion and thus the higher the density of surface defects, which could give rise to a higher number of nonradiative decay paths. Nevertheless, the influence of the spatial confinement increasing the overlap between the electron and hole wavefunctions, and thus increasing the radiative recombination probability,[34] cannot be discarded.

We complete our analysis by studying the effect of the matrix in which the nanocrystals are embedded on their decay dynamics. In Figure 4c we show the PL spectra of $MAPbI_3$ crystallites grown in TiO_2 (orange line) and SiO_2 (purple line) scaffolds of similar average pore size and distribution, while Figure 4d displays the corresponding characterization of the decay dynamics. While the normalized photoemission intensity spectra are reasonably similar, as expected for collection of crystallites of similar size distribution, it can be seen that the decay rate is approximately four times faster in the TiO_2 scaffold than in the SiO_2 one. As the QY measured for nanocrystals confined in SiO_2 cages is similarly small ($QY_{SiO2} \approx 1\%$), the significant difference in Γ can only be due to an increase of Γ_{NR} when a TiO_2 matrix is used. In this regard, the possibility to transfer photocarriers to the TiO_2 matrix, which does not exist in the case of SiO_2, might manifest itself through a faster decay. At the same time, since $QY = \frac{\Gamma_R}{\Gamma_{NR}+\Gamma_R} \approx \frac{\Gamma_R}{\Gamma_{NR}}$, the fact that the QY remains basically constant indicates that somehow Γ_R is also being accelerated in TiO_2 matrices. The expected ratio between the Γ_R attained for two similar emitters located in different media $\frac{\Gamma_{R,i}}{\Gamma_{R,j}}$ is roughly proportional to the fifth power of the quotient of the refractive indexes, $\frac{n_i}{n_j}$, of such media.[35,36] In our case, refractive indexes should be estimated as the average between those of perovskite nanocrystals and the metal oxide scaffold in each case. By using Bruggeman effective medium approximation, and assuming a 50% fill factor, we obtain $\frac{\Gamma_{R,TiO2}}{\Gamma_{R,SiO2}} \approx \left(\frac{n_{TiO2}}{n_{SiO2}}\right)^5 = 3.5$. This ratio is similar to the $\frac{\Gamma_{TiO2}}{\Gamma_{SiO2}} \approx \frac{\Gamma_{NR,TiO2}}{\Gamma_{NR,SiO2}} \approx 4$ experimentally determined. Hence, the similar QY observed for similar nanocrystals emitting from the different matrices employed could be explained by the compensating effect of simultaneously faster nonradiative and radiative decay rates.

In summary, we have demonstrated a simple, reliable, and reproducible method to obtain solid dispersions of methyl ammonium lead iodide nanocrystals with tetragonal crystal

structure embedded in the periodic porous mesostructure of metal oxide thin films of high optical quality. By synthesizing the perovskite inside the interconnected array of nanocages of the host film, and by using matrices with pores of different average size, we show fine tuning of the static and dynamic photoemission properties of the crystallites in a wide spectral range. This method can be easily extended to other hybrid perovskites, evidence of which is provided as Figure S3 (Supporting Information). Such control over the optical properties arise from the strong quantum size effects characteristic of semiconductor nanocrystals of dimensions comparable to the exciton Bohr radius, as we show by fitting our experimental data to canonical expressions derived for that regime. We believe our results open interesting possibilities for the application of $CH_3NH_3PbI_3$ perovskite nanocrystals in optoelectronics as they show they can be synthesized within films and, due to confinement effects, become stable visible light emitting materials at the desired frequency range. Besides, they show a remarkably fast photoactivation compared to dense films. Our synthetic route also provides a material with a tuneable electronic bandgap, which may be of interest for the development of tandem solar cells based on $CH_3NH_3PbI_3$, which present superior photovoltaic performance than those formed by Br or Cl.

Experimental Section

Synthesis of Periodically Mesostructured Scaffolds: The preparation of mesoporous structures with different well-defined pore size was made by using a supramolecular templating approach reported on previous works. The synthesis is based on the hydrolysis and condensation (sol–gel method) of TiO_2 and SiO_2 precursors around a well-defined 3D arrangement of an organic templating agent. After the removal of the organic pattern by thermal treatment, an oxide mesostructure film arises with an open, ordered, and interconnected network of pores with regular shape. This method allows controlling the pore size by changing the organic template.

In this work, several surfactants were used as templating agents to obtain TiO_2 mesoporous films. First, a dispersion of $TiCl_4$ (Sigma-Aldrich) in ethanol (EtOH, VWR Chemical) was prepared in a Ti:EOH 1:40 molar ratio. Then the surfactant was added under strong stirring. The surfactants used in this work were: CTAB (Aldrich), two different triblock copolymers (pluronics F127 and P123), and alkylpoly(ethylene oxide) (Brij 58, Sigma). The surfactant/Ti ratio (in moles) was: 0.100 in CTAB, 0.05 in Brij 58, 0.005 in F127 and P123. The largest pore size was obtained using a combination of the previous method and phase separation. In this case, the dispersion was prepared in 1-butanol using both $TiCl_4$ and F127 in the same molar ratio described above. Thus, 0.24 g of polypropylene glycol 4000 (PPG, Alfa Aesar GMBH&Co KG) and 4 mL of tetrahydrofuran (Panreac) were added to the dispersion. Finally, H_2O was added to the above described dispersion in a H_2O/Ti molar ratio of 10. SiO_2 mesoporous films were prepared in the same way described above starting from a prehydrolyzed tetraethylortosilicate dispersion as inorganic source (instead of $TiCl_4$).

All dispersions were aged during 2 d previously to be deposited. Deposition of the precursors was made in low fluorescence slides by dip coating method. The withdrawal speed, 2 mm s^{-1}, was adjusted to obtain a 200 nm thickness film (100 nm for the cases of F127 + PPG-based TiO_2, and CTAB-based SiO_2 scaffolds). Humidity in the deposition chamber was kept constant at values between 40% and 50%. After deposition, the humidity was increased to 80% for 10 s, and then the fresh films were placed in a chamber with 50% humidity during 24 h. Next, samples were kept at 60 °C during 24 h and then at 120 °C for another 24 h. These steps were needed in order to consolidate the oxide network around the organic template. Finally, the latter was removed by treating the films during 1 h at 350 °C (ramp of 1 °C min^{-1}). For the cases of F127 + PPG-based TiO_2 and CTAB-based SiO_2 scaffolds, the deposition process was repeated in order to achieve films around 200 nm thick.

Synthesis of Perovskite Precursors: $CH_3NH_3PbI_3$ perovskite precursors solution was prepared following a well-established procedure,[37] which involves the nonstoichiometric mixture of methylammonium iodide (MAI) salt and lead chloride (268690, Sigma-Aldrich). In order to obtain high reproducibility in the photophysical properties of the $CH_3NH_3PbI_3$ synthesized within the pores, it is critical to have a protocol for the homemade MAI powder production. Concerning this point, a commercial solution of 12 mL of methylamine in ethanol (534102, Sigma-Aldrich) was diluted in 50 mL of absolute ethanol and stirred for 10 min. Then, 5 mL of hydriodic acid aqueous solution (210021, Sigma-Aldrich) was slowly added avoiding an excessive heating produced by exothermic reaction, employing an ice-water cooling bath. Reaction completion required stirring for 30 min. Afterward, a rotary evaporator was employed to concentrate the light yellow solution until a white MAI powder was obtained. In order to remove impurities, the white crystals were washed several times with anhydrous diethyl ether and dried at 70 °C in a vacuum oven overnight. Finally, to obtain the final semitransparent yellow $CH_3NH_3PbI_3$ perovskite solution, MAI and $PbCl_2$ were dissolved in anhydrous *N*,*N*-dimethylformamide (D4551, Sigma-Aldrich) at a 3:1 molar ratio up to final concentrations between 20 and 40 wt%.

A similar procedure was followed to attain the $CH_3NH_3PbBr_3$ perovskite precursor solution. Methylammonium bromide (MABr) was prepared by adding 8 mL methylamine and 2.83 mL hydrobromic acid (18739, Fluka) solutions to 22 mL of absolute ethanol. Same washing and recrystallization processes as in the MAI powder case were adopted. The as-prepared MABr powder was dissolved together with $PbBr_2$ (211141, Sigma-Aldrich) at a 3:1 molar ratio in anhydrous *N*,*N*-dimethylformamide, to give a transparent colorless solution with a concentration of 20 wt%.

Infiltration of Inorganic Mesoporous Structures: Infiltration of periodic porous mesostructures with $CH_3NH_3PbI_3$ and $CH_3NH_3PbBr_3$ was carried out by sequentially spin coating the perovskite precursor solutions on top of the supramolecularly templated mesoporous scaffolds deposited on low fluorescence substrates. Perovskite formation was completed by treating the samples 1 h at 100 °C. To avoid the deposition of a perovskite capping layer (that could mislead in the analysis of the photoluminescence measurements), we adjusted the $CH_3NH_3PbI_3$ solution concentration and spin coating deposition parameters (see Figure S1, Supporting Information). We found that a concentration of 20 wt% and a final rotation speed of 5000 rpm were the optimized parameters, being appropriate also for the $CH_3NH_3PbBr_3$ perovskite. This method assures that perovskite nanocrystals are exclusively grown within the inorganic scaffold.

Structural Characterization: For TEM characterization cross-section lamellas were prepared using a dual focused ion beam Helios Nanolab 650 (FEI company). To get information about the microstructure and to obtain the element distribution maps, an FEI Tecnai field emission gun scanning transmission electron microscope, mod. G2F30 with an S-Twin objective lent, operated at 300 kV, with 0.2 nm point resolution, and equipped with an HAADF detector from Fischione with 0.16 nm point resolution, and an EDX detector SSD mod. INCA X-Max 80 was used. The Ti and Pb elemental maps were obtained by EDX spectroscopy using the characteristics X-ray photons for Ti Kα (4.5 keV) and Pb Lα1 (10.55 keV) and scanning an electron probe with a diameter of less than 1 nm size and registering the EDX spectra in the same region as showed in the HAADF image. Gatan Digital Micrograph software was used to acquire images and perform further image processing. The software used to estimate the nanocrystal size distribution from the different electron microscopy images obtained was ImageJ.

XRD measurements were collected in a PHILIPS X'pert PRO diffractometer. Acquisition of the samples was taken in the 5–90 2θ range with a 0.05 step.

Optical Characterization: PL measurements were carried out in front-face configuration (collection at an angle of 11.25°) with a commercial

fluorimeter (Fluorolog-3 from Horiba). Excitation was performed with a monochromated xenon lamp and the emitted light was collected with a photomultiplier tube after passing through a second monochromator. The spot of the excitation beam was 1 cm^2 large. The shape of the PL spectrum from the sample was constant as the spot was moved across evidencing its homogeneity.

PL mapping was carried out in a set-up in which a continuous wave pump laser beam was focused with a $f = 10$ cm achromatic lens, serving also as collection optics, to a 250 μm^2 spot on the sample which was mounted on an X–Y micrometer stage. PL spectra were collected with a fiber coupled spectrophotometer (Ocean Optics USB-2000). Photoactivation measurements were carried out in the same setup.

Lifetime measurements were conducted coupling a tunable pulsed light source (Fianium SC400) delivering 900 ps pulses with a repetition rate variable between 2 and 10 MHz to the former equipment and using a time-correlated single photon counting module (Fluorohub). The excitation wavelength was 532 nm. Experimental decay curves were deconvoluted with the instrument response function and fitted with the DAS6 software to a normal distribution of lifetimes

$$I(t) = \int_0^\infty \rho(\Gamma) e^{-\Gamma t} d\Gamma \quad (4)$$

where in this case $\rho(\Gamma)$ is a top-hat distribution characterized by a mean value and a full width at half maximum $\Delta\Gamma$. Quantum yield measurements were carried out using an integrating sphere (Quanta-ϕ), also coupled to the former equipment, using a $\lambda = 532$ nm excitation line and collecting light emitted at all wavelengths. A protocol based on the subtraction of the absorption and the concomitant photoemission attained under indirect illumination from the values attained for both parameters under direct illumination was followed.[38]

Supporting Information

Supporting Information is available from the Wiley Online Library or from the author.

Acknowledgements

The research leading to these results had received funding from the European Research Council under the European Union's Seventh Framework Programme (FP7/2007-2013)/ERC Grant Agreement No. 307081 (POLIGHT) Project, the Spanish Ministry of Economy and Competitiveness under Grant No. MAT2014-54852-R. M.A. is grateful to "La Caixa" Foundation for its financial support. A.R. acknowledges the Spanish Ministry of Economy and Competitiveness for funding through an FPI program. Lamellae preparation was conducted in the "Laboratorio de Microscopias Avanzadas" at "Instituto de Nanociencia de Aragón-Universidad de Zaragoza." Authors acknowledge the LMA-INA for offering access to their instruments and expertise.

Received: December 22, 2016
Revised: January 19, 2017
Published online: March 3, 2017

[1] A. D. Yoffe, *Adv. Phys.* **1993**, *42*, 173.
[2] L. C. Schmidt, A. Pertegás, S. González-Carrero, O. Malinkiewicz, S. Agouram, G. Mínguez Espallargas, H. J. Bolink, R. E. Galian, J. Pérez-Prieto, *J. Am. Chem. Soc.* **2014**, *136*, 850.
[3] S. T. Ha, X. Liu, Q. Zhang, D. Giovanni, T. C. Sum, Q. Xiong, *Adv. Opt. Mater.* **2014**, *2*, 838.
[4] F. Zhang, H. Zhong, C. Chen, X.-G. Wu, X. Hu, H. Huang, J. Han, B. Zou, Y. Dong, *ACS Nano* **2015**, *9*, 4533.
[5] H. Huang, A. S. Susha, S. V. Kershaw, T. F. Hung, A. L. Rogach, *Adv. Sci.* **2015**, *2*, 1500194.
[6] Y. Hassan, Y. Song, R. D. Pensack, A. I. Abdelrahman, Y. Kobayashi, M. A. Winnik, G. D. Scholes, *Adv. Mater.* **2016**, *28*, 566.
[7] S. Bai, Z. Yuan, F. Gao, *J. Mater. Chem. C* **2016**, *4*, 3898.
[8] S. D. Stranks, H. J. Snaith, *Nat. Nanotechnol.* **2015**, *10*, 391.
[9] F. Deschler, M. Price, S. Pathak, L. E. Klintberg, D.-D. Jarausch, R. Higler, S. Hüttner, T. Leijtens, S. D. Stranks, H. J. Snaith, M. Atatüre, R. T. Phillips, R. H. Friends, *J. Phys. Chem. Lett.* **2014**, *5*, 1421.
[10] G. Xing, N. Mathews, S. S. Lim, N. Yantara, X. Liu, D. Sabba, M. Grätzel, S. Mhaisalkar, T. C. Sum, *Nat. Mater.* **2014**, *13*, 476.
[11] Z.-K. Tan, R. S. Moghaddam, M. L. Lai, P. Docampo, R. Higler, F. Deschler, M. Price, A. Sadhanala, L. M. Pazos, D. Credgington, F. Hanusch, T. Bein, H. J. Snaith, R. H. Friend, *Nat. Nanotechnol.* **2014**, *9*, 687.
[12] Y. Ling, Z. Yuan, Y. Tian, X. Wang, J. C. Wang, Y. Xin, K. Hanson, B. Ma, H. Gao, *Adv. Mater.* **2015**, *28*, 301.
[13] M. Cadelano, V. Sarritzu, N. Sestu, D. Marongiu, F. Chen, R. Piras, R. Corpino, C. M. Carbonaro, F. Quochi, M. Saba, A. Mura, G. Bongiovanni, *Adv. Opt. Mater.* **2015**, *3*, 1557.
[14] D. N. Dirin, L. Protesescu, D. Trummer, I. V. Kochetygov, S. Yakunin, F. Krumeich, N. P. Stadie, M. V. Kovalenko, *Nano Lett.* **2016**, *9*, 5866.
[15] V. Malgras, S. Tominaka, J. W. Ryan, J. Henzie, T. Takei, K. Ohara, Y. Yamauchi, *J. Amer. Chem. Soc.* **2016**, *138*, 13874.
[16] Z. Chen, Z.-G. Gu, W.-Q. Fu, F. Wang, J. Zhang. *ACS Appl. Mater. Interfaces* **2016**, *8*, 28737.
[17] G. J. D. Soler-Illia, C. Sanchez, B. Lebeau, J. Patarin, *Chem. Rev.* **2012**, *102*, 4093.
[18] M. Hirasawa, T. Ishihara, T. Goto, K. Uchida, N. Miura, *Phys. B* **1994**, *201*, 427.
[19] V. D'Innocenzo, G. Grancini, M. J. P. Alcocer, A. R. S. Kandada, S. D. Stranks, M. M. Lee, G. Lanzani, H. J. Snaith, A. Petrozza, *Nat. Commun.* **2014**, *5*, 3585.
[20] E. Menéndez-Proupin, P. Palacios, P. Wahnón, J. C. Conesa, *Phys. Rev. B* **2014**, *90*, 045207.
[21] J. Ma, L.-W. Wang, *Nano Lett.* **2015**, *15*, 248.
[22] A. Buin, R. Comin, A. Ip, H. Sargent, *J. Phys. Chem. C* **2015**, *119*, 13965.
[23] Y. Kayanuma, *Phys. Rev. B* **1988**, *38*, 9797.
[24] L. E. Brus, *J. Chem. Phys.* **1984**, *80*, 4403.
[25] Al. L. Éfros, A. L. Éfros, *Sov. Phys. Semicond.* **1982**, *16*, 1209.
[26] P. Umari, E. Mosconi, F. De Angelis, *Sci. Rep.* **2014**, *4*, 4467.
[27] J. Even, L. Pedesseau, C. Katan, *J. Phys. Chem. C* **2014**, *118*, 11566.
[28] G. Giorgi, K. Yamashita, *J. Phys. Chem. Lett.* **2016**, *7*, 888.
[29] J. F. Galisteo-López, M. Anaya, M. E. Calvo, H. Míguez, *J. Phys. Chem. Lett.* **2015**, *6*, 2200.
[30] Y. Tian, M. Peter, E. Unger, M. Abdellah, K. Zheng, T. Pullerits, A. Yartsev, V. Sundström, I. G. Scheblykin, *Phys. Chem. Chem. Phys.* **2015**, *17*, 24978.
[31] D. W. de Quilettes, W. Zhang, V. M. Burlakov, D. J. Graham, T. Leijtens, A. Osherov, V. Bulovic, H. J. Snaith, D. S. Ginger, S. D. Stranks, *Nat. Commun.* **2016**, *7*, 11683.
[32] S. D. Stranks, V. M. Burlakov, T. Leijtens, J. M. Ball, A. Goriely, H. J. Snaith, *Phys. Rev. Appl.* **2014**, *2*, 034007.
[33] T. Takagahara, *Phys. Rev. B* **1987**, *36*, 9293.
[34] V. K. Ravi, A. Swarnkar, R. Chakraborty, A. Nag, *Nanotechnology* **2016**, *27*, 325708.
[35] E. Yablonovitch, T. J. Gmitter, R. Bhat, *Phys. Rev. Lett.* **1988**, *61*, 2546.
[36] B. Henderson, G. F. Imbusch, *Optical Spectroscopy of Inorganic Solids*, Oxford University Press, New York, USA **1989**, p. 146.
[37] M. M. Lee, J. Teuscher, T. Miyasaka, T. N. Murakami, H. Snaith, *Science* **2012**, *338*, 643.
[38] D. O. Faulkner, J. J. McDowell, A. J. Price, D. D. Perovic, N. P. Kherani, G. A. Ozin, *Laser Photonics Rev.* **2012**, *6*, 802.